Materials Characterization 200 (2023) 112907

Contents lists available at ScienceDirect

Materials Characterization

journal homepage: www.elsevier.com/locate/matchar

An investigation of the fatigue behavior of additively manufactured laser shock peened AlSi7Mg surfaces

Milad Hamidi Nasab [a,c,*], Maurizio Vedani [c], Roland E. Logé [a], Navid Sohrabi [a], Amir Mohammad Jamili [a], Anton du Plessis [b], Stefano Beretta [c]

[a] Thermomechanical Metallurgy Laboratory – PX Group Chair, Ecole Polytechnique Fédérale de Lausanne (EPFL), CH-2002 Neuchâtel, Switzerland
[b] Research Group 3DInnovation, Stellenbosch University, Stellenbosch 7602, South Africa
[c] Department of Mechanical Engineering, Politecnico di Milano, Milano, Italy

ARTICLE INFO

Keywords:
Additive manufacturing
Laser powder bed fusion
Laser shock peening
Residual stresses
Fatigue

ABSTRACT

In the recent years, laser powder bed fusion of aluminum alloys has attracted attention due to their capacity for applications in the biomedical, aerospace, and industrial sectors. This is due to the combined capability of the laser powder bed fusion process and aluminum alloys in producing complex shapes with high performance associated with light-weight designs. Despite their potential, laser powder bed fusion suffers from residual stresses, surface irregularities and sub-surface defects which limit their full exploitation in fatigue-sensitive applications. Consequently, post-processing methods such as laser shock peening can be employed to counter these short-comings. This paper reports the effect of laser shock peening on the fatigue life of AlSi7Mg fabricated via laser powder bed fusion. Laser shock peening induced substantial improvement (more than 50%) in the fatigue life when compared to as-built parts. The improvements were attributed to the closure of surface and sub-surface pores, surface treatment and in particular, compressive residual stresses. The effect of laser shock peening was investigated through systematic analyses of surface roughness, hardness and residual stresses. Further, a simple fracture mechanics model was utilized to predict the effect of induced compressive residual stresses as the principal contributor to the corresponding fatigue improvement.

1. Introduction

Laser Powder Bed Fusion (L-PBF) is an Additive Manufacturing (AM) process in which a laser selectively melts layers of metal powder according to a given scanning strategy [1–3]. In the past two decades, L-PBF has attracted attention in both industry and academia as a new fabrication method enabling the production of complex geometries with shorter lead time and low material wastage. Despite these advantages, high surface roughness, formation of defects such as porosity [4,5] and the presence of high levels of tensile residual stresses (TRS) [6] significantly impact the fatigue properties and impede broad industrial application of L-PBF parts [5,7–13]. Various strategies have been developed in the past 10 years to address these issues, most of them focusing on post-processing treatment of L-PBF parts [14]. These include volumetric treatments such as heat treatment for residual stress relief, Hot Isostatic Pressing (HIP) for porosity reduction, and surface treatments such as machining [9,15,16].

The efficiency of HIP has been largely confirmed for the removal of gas pores, lack-of-fusion defects, and large interconnected porosity. However, Du Plessis and Macdonald [17] showed that HIP was not effective in removing all the pores, with some pores shrinking beyond the detection limit, re-opening upon subsequent heat treatment. Besides, HIP is incapable of closing sub-surface pores connected to the surface because of the presence of an opening to the surface during the treatment [18]. Such porosities act as near-surface defects that are particularly detrimental to the fatigue properties ("killer" defects), critically contributing to the crack initiation in fatigue [19]. A previous work investigated the effect of stress, surface and volume defects on the fatigue properties of as-built AlSi7Mg and demonstrated that the sub-surface pores act as stress raisers, favoring crack nucleation [7].

Surface treatments such as machining, electro-chemical machining remove surface features such as notches

* Corresponding author at: Rue de la Maladière 71b, 2002 Neuchâtel, Switzerland.
E-mail address: Milad.hamidinasab@epfl.ch (M. Hamidi Nasab).

https://doi.org/10.1016/j.matchar.2023.112907
Received 4 November 2022; Received in revised form 20 January 2023; Accepted 7 April 2023
Available online 8 April 2023

and favor local stress concentration and fatigue crack initiation [20]. In order to further enhance the fatigue properties, introduction of compressive residual stress (CRS) in the near-surface region through specific surface treatments such as sandblasting [21], shot peening [22] or laser shock peening (LSP) [23–27] have demonstrated efficiency. In sandblasting and shot peening, the high impact of each high-pressure stream of abrasive media or shots on metallic or ceramic balls, respectively, generates compressive residual stress via plastic deformation in the near-surface region [28,29]. In addition, depending on the process, porosity closure in the sub-surface region [30]. Although it has been reported that shot peening has influence in the improvement of fatigue life [29,30], increasing the surface roughness and cracks forming on the surface in the first material has adverse effect on the fatigue performance of the part [31].

Among other post-processing treatments, LSP is a well-established post-processing method to improve the fatigue performance of metal parts in aerospace applications such as jet engines and compressor blades [23]. During LSP, high-intensity pulsed laser generates a hot plasma whose expansion under the water layer creates a pressure wave that propagates into the material, resulting in compression to a depth that varies depending on the LSP process parameters [20,22,23,33]. In industrial applications, geometric features such as small fillet radii, edges and holes are critical stress concentration locations. Unlike shot peening, LSP can be selectively applied to localized fatigue 'hot spots' in order to induce compressive residual stresses and enhance the fatigue life accordingly [20,22,33,34]. Further, LSP imposes higher CRS with respect to shot peening, increasing the effective depth of the affected area [35].

Most prior research works reported an increase in fatigue life of various LSP-treated alloys compared to as-built (AB) L-PBF condition or wrought material [23,24,33,35,36]. This is attributed to the introduction of the compressive residual stresses with deep layer extension, CRS and to the microstructural changes (e.g., grain refinement and higher dislocation density) [24,33,37–47] that LSP induces in the surface and near-surface layers. Further, LSP demonstrated the ability to close surface (sub-)pores [48], typically acting as crack initiation sites. Lu et al. reported a 23.6% increase in fatigue strength of LSP-treated TC17 titanium alloy compared to AB condition [24]. Hackel et al. observed that the peening provided a fatigue strength improvement in the range of 60% for notched L-PBF 316L specimens [23]. Ye et al. reported improvement in fatigue life of 316L SS samples by about 12.5% [49]. Huang et al. measured increase of 14–87.5% in fatigue life for LSP-treated TC4 titanium specimens depending on the applied laser power densities [50], while according to Yang et al. fatigue life increased by about 2.5 times in the high-cycle fatigue (HCF) regime after LSP of Ti6Al4V alloy [51].

However, contradictory reports were made by Qiao et al. and Jiang et al. who observed decrease in fatigue life of LSP-treated specimens of 2024-T351 aluminum alloy and Ti6Al4V alloy under high cycle and ultra-high cycle fatigue regimes, respectively [36,52]. With most of the crack initiation sites being located in the subsurface region of the specimen after LSP, Qiao et al. attributed this decrease in HCF strength to the tensile residual stresses (TRS) induced in the region to balance the surface compressive residual stresses, favoring crack initiation and growth through increase of the mean stress during fatigue loading [52]. Jiang et al. made similar observation, highlighting that fatigue cracks initiated from internal defects at some laser-shock peened specimens. Additionally, an increase in surface roughness after LSP, which is detrimental to fatigue strength, especially in the UHCF regime [36].

The present paper aims to evaluate the effect of LSP on the fatigue properties of AlSi7Mg specimens manufactured by L-PBF, which, to our knowledge, have not yet been documented in the literature using different sets of L-PBF process parameters, effect of types of surface defects (e.g., attached particles, spatters, pores), surface roughness and sub-surface porosities) are combined in order to evaluate the effects of such (sub-)surface features on the LSP process efficiency, post-LSP surface morphology, microstructure, residual stress distribution and resulting fatigue behavior.

2. Materials and methods

2.1. Material and sample manufacturing

AlSi7Mg samples in this study were manufactured by L-PBF utilizing Renishaw AM250 system (Wotton-under-Edge, UK) with a single-mode pulsed fiber laser with a maximum power of 200 W, focused spot size of 75 μm. The powder was commercial gas atomized AlSi7Mg (A357) supplied by LPW Technology (LPW Technology Ltd., Runcorn, UK), whose chemical composition is reported in Table 1.

Cuboid specimens with size of 15 mm × 15 mm × 10 mm were printed on the reduced build volume (RBV) platform in a circular distribution with equal radial distance (50 mm) and oriented to minimize the axis of the laser source to avoid the effect of position dependence properties. All samples were printed with identical process parameters (referred as default in the following experiments) except for contour process parameters in order to generate different surface features and porosity at sub-surface location at the contour region. The energy input using a vector (e.g. contour energy, E_L) for L-PBF systems equipped with pulsed laser can be calculated through the laser power (P_L), the exposure time (t_s) and the point distance (P_d) according to Eq. 1

$$E_L = \frac{P_L . t_s}{P_d} \quad (1)$$

The process parameters of the reference and contours for the manufacturing of the samples are presented in Table 2 and Table 3, respectively. t_L, D_y, and d_0 are the powder layer thickness, hatch distance and spot size, respectively. Based on the hatch distance and spot size given in Table 2, we can observe a significant overlap of the printing tracks is expected. A relatively large overlapping between tracks (both laterally and in depth) is important to obtain the homogeneity of the structure and prevent defects related to lack of fusion and cracking. A number of energy densities were chosen based on results previously published by the authors [7] to deliberately introduce distinct surface features in order to evaluate their role in the effect of surface features on the fatigue behavior of AlSi7Mg alloy obtained by L-PBF.

2.2. Laser shock peening (LSP)

Once the cube specimens were manufactured via L-PBF, they were subjected to LSP in the in-house-built LSP experimental setup, one utilizing Nd:YAG GAIA-HP laser source (Thales Group, France) operating at 1064 nm wavelength with a pulse duration of 6.3 ns under water confinement. A laser spot of 1 mm with an energy of 1 J and pulse frequency of 5 Hz was chosen based on previous investigations on a wide range of metallic alloys [35,46,47]. This gave power density of 1.8 GW/cm². Utilizing the empirical equation P(GPa) = $1.75\sqrt{I_0}$ (GW/cm²) from [53], the pressure at the surface of the part was estimated at 2.4 GPa. The beam spatial energy distribution was set to top-hat with near-Gaussian pulse shape. The LSP treatments

Table 1
Chemical composition of the AlSi7Mg powder (wt%).

Si	Mg	Mn	Fe	Ti	Zn	Cu	Al
6.7–7.3	0.25–0.45	0.5–0.6	0.14	0.08–0.12	0.09	0.04	bal.

Table 2
Core process parameters used in the build of the AlSi7Mg samples.

P_L (W)	t_s (μs)	P_d (μm)	T_L (μm)	D_h (μm)	r_0 (μm)
200	140	80	25	100	75

Table 3
Contour process parameters used in the build of the AlSi7Mg samples.

Surface code	P_L (W)	t_s (μs)	P_d (μm)	E_L (J/m)
S01	200	140	80	350
S05	150	42	50	125
S07	100	42	50	83

were applied to the side vertical surfaces of 9 cube specimens (three specimens per surface code) with a positive offset of 50% applied to the surface contour scan, and each surface code was evaluated to determine the distribution of the residual stress depth profile.

2.3. Residual stress measurements

Hole Drilling Method (HDM) was employed for the residual stress measurement of the AB and LSP surfaces using RESTAN-MTS 3000 (SINT Technology, Italy) hole drilling system. The technique is widely used for the determination of in-depth residual stress profiles in parts subjected to high energy impact surface treatments [54]. The measurements were made according to the ASTM standard E837 [55]. In this process, a 1.8 mm diameter hole with 1 mm depth is drilled into the specimen and the strain from residual stress relaxation due to drilling is measured by strain gauge rosettes with three grids. Residual stress measurements of the surfaces produced according to the parameter sets (S01, S05, and S07) in AB and LSP conditions with three repetitions (n = 18 measurements total). A variable depth increment was applied to obtain more precise results near the surface region. From the surface down to 100 μm depth, the measurements were carried out every 10 μm; from 0.1 mm to 0.5 mm in depth, the measurements were every 25 μm; and from 0.5 mm to 1 mm, every 50 μm.

2.4. Microhardness measurements

Microhardness depth profiles were collected on the LSP cross sections to investigate the microhardness evolution in depth from the surface induced by the LSP process in the specimens. Vickers microhardness was measured using a 100 g load and 12 s holding time at room temperature, using a Q10A+ instrument (Qness GmbH, Germany). The distance between two consecutive indentations following the recommendations of ISO 6507-1. Three rows per specimen (S01, S05, and S07), 30 indentations separated by a 25 μm gap were made along the specimen depth. The average microhardness and the corresponding standard deviation were obtained by considering three measurements at each depth per specimen.

2.5. Morphological and texture analysis of the surfaces

A non-contact laser-based metrology was employed to investigate the effect of LSP on the morphology of the L-PBF AB surfaces. The measurements were obtained by employing a Keyence VK-X1100 Confocal microscope equipped with semi-conductor laser with a resolution of 1 nm. The specimens were measured utilizing a 10× (numerical aperture 0.3) objective and a total area of 2.9 mm × 2.9 mm. Nine acquisitions, each 1 mm × 1 mm in size, collected and stitched together with 15% overlap. For areal surface parameter calculation, the raw data were subjected to form removal, followed by a spatial filter (median denoising 5 × 5) to remove spurious points. Subsequently, a Gaussian low-pass filter with a 2.9 mm cut-off was applied equal to the length of the field of view to eliminate the waviness scales larger than the field of view, thus obtaining S-F surface. Afterwards, a Gaussian filter with 0.8 mm cut-off was applied to circumvent the waviness scales, obtaining S-L surface. The set of surface parameters was selected based on the specific aim of the surface analysis in agreement with previous published works [56]. The areal parameters were computed based on the ISO 25178-2 standard [57].

Images of the surface profiles were obtained from the samples sectioned perpendicular to the build direction (z axis) after grinding, polishing, and etching by Keller's reagent. The images were taken employing a Nikon Eclipse LV150NL optical microscope (OM) to acquire a detailed evaluation of the sub-surface. Particular attention was paid to the microstructure in the regions intersecting the surface profile and subjected to the thermal heat affected zone [58]. Further microstructural analysis was done using Zeiss-Gemini SEM scanning electron microscope (SEM) and EDX analysis on the LSP surfaces investigating possible contaminations as a result of the LSP process. Electron Backscatter Diffraction (EBSD) maps were acquired close to surface sections along the build direction with the same microscope equipped with Symmetry camera and Aztec acquisition software (Oxford Instruments). The maps were acquired at 25 kV with the step size of 0.5 μm with the acquisition of 200 Hz with the tilt of 70°, binning 2, and mode speed 1.

2.6. Fatigue testing

The three sets representing the surface codes (S01, S05, and S07) were selected due to their potential to improve the fatigue performance induced by LSP with respect to the AB surfaces, and investigated in a study published by the authors [7].

Ten three-point bending fatigue samples per surface code were then fabricated using the process parameters for the core and contour scans presented in Table 2 and Table 3 respectively, according to the design depicted in Fig. 1a. The fatigue specimens were printed horizontally with their surface of interest perpendicular to the build direction (Fig. 1b). In order to accelerate the test and reduce the experimental effort to evaluate the effect of LSP on the AB surfaces, the corresponding fatigue properties, the grouping approach proposed by Boni et al. [59] was employed. Prior to the LSP treatment, the fatigue specimens were subjected to aging at 160 °C for 4 h (T5 heat treatment) [60]. Consequently, the specimens went through LSP treatment with the parameters in Sect. 2.2. The LSP treatment was applied on the central area of the fatigue specimen's curve with a treatment length of 12 mm (Fig. 1c and d).

Three-point bending fatigue tests were performed in load-control mode utilizing a MTS Acumen 3 electrodynamic test equipment with a maximum load capacity of 3 kN. The fatigue tests were performed on LSP and AB samples with a load ratio R of 0.1 at ambient temperature conditions, at stress ranges, with maximum applied stresses varying from 200 to 300 MPa, to investigate fatigue life in the range of 10^4 cycles to the run-out limit, which was set to 5×10^6 cycles under frequency of 30 Hz. Finally, post-mortem fractography analysis was performed on all the broken fatigue specimens in the SEM to identify fracture surface features at the crack nucleation, the extent of crack growth and to statistically analyse the extents.

2.7. X-ray tomography investigation

To measure the porosity in the AB and LSP fatigue specimens, X-ray tomography was applied using a typical laboratory micro-CT equipment at the Elettra TomoLab facility [61]. Two fatigue samples per category

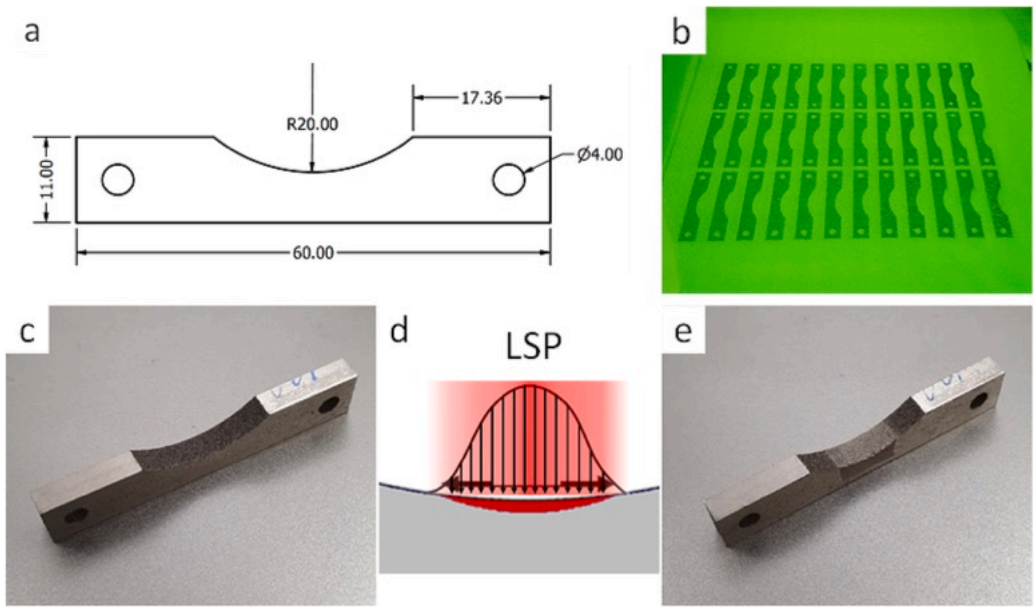

Fig. 1. (a) Geometry of the three-point bending specimens in the L-PBF AlSi7Mg, (b) printing with the surface of interest being parallel to the build direction, (c) AB and LSP-treated specimens, (d) schematic of the LSP process on the surface of the specimens.

(S05, S010, and S07) and condition (AB and LSP-treated) were subjected to non-destructive X-ray tomography prior to the fatigue tests.

The voxel size of the micro-CT scans was selected as 15 μm, allowing analysis of pores and surface features at this value, and providing a view of the development of porosity in the samples' critical surface and sub-surface. The parameters were set at 150 kV and 100 μA for X-ray generation with a 0.5 mm copper filter. The samples were loaded in the micro-CT with their long axis vertical and rotated around this axis during scanning. A full 360-degree rotation was used for scanning in 2000 steps, at each position the first image was discarded and the subsequent 3 images were averaged. Detector shift was enabled to minimize ring artifacts [12].

3. Results

3.1. Morphology of the surfaces

The representative SEM images of the AB and LSP-treated surfaces are presented in Fig. 2 and Fig. 3, respectively. The most typical features of the AB vertical surface are the presence of partially fused spatter and powder particles, showing variability in their size and distribution. The different AB surfaces demonstrated differences in terms of type, size and amount of the above features. A substantially denser surface was observed on S01 specimen

lar spatter (see the green arrows in Fig. 2) and partially fused metal powder particles (as shown with the blue dotted rectangles in Fig. 2). In samples with lower contour energy (S05 and S07 samples), a few cavities on surface were observed (shown with the red arrows in Fig. 2b and 2c) as a result of insufficient energy density, probably due to the attached particles avoiding the melting of the patterns. Further, the S07 surface shows a higher number of attached particles on the surface which could be due to the lower contouring energy. Plateau-Rayleigh instability could be another reason due to the corresponding scanning velocities.

Upon application of LSP on the AB surface, the observed features in Fig. 2 were substantially altered depending on the impact of varied LSP, resulting in removal or deformation of the above-mentioned features. LSP treatments led to the removal of partially fused powders, providing the smoothest S01 surface (Fig. 3a), while incomplete removal of fused particles in S05 and S07 surfaces (Fig. 3b and 3c). In these LSP treatments higher surface features are visible on the surface, which could be attributed to already existing sub-surface pores which are exposed after the subsequent LSP treatment.

Taking a closer look at the magnified LSP-ed surfaces (Fig. 3d and 3e), a surface texture is revealed which could be an indication of the presence of plastic deformation during LSP process. EDS analysis of the LSP-ed

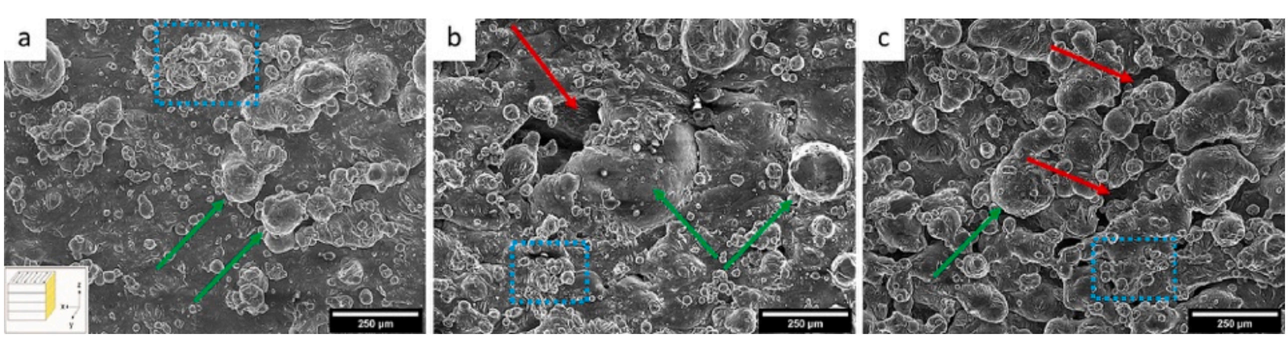

Fig. 2. SEM images of the AB surfaces (parallel to build direction) printed with different contour energy by L-PBF: (a) S01, E_L = 350 J/m; (b) S05, E_L = 125 J/m; (c) S07, E_L = 83 J/m. The images show the presence of spatters (green arrows), partially fused powder (blue dotted rectangle) and cavities (red arrows) on the surface.

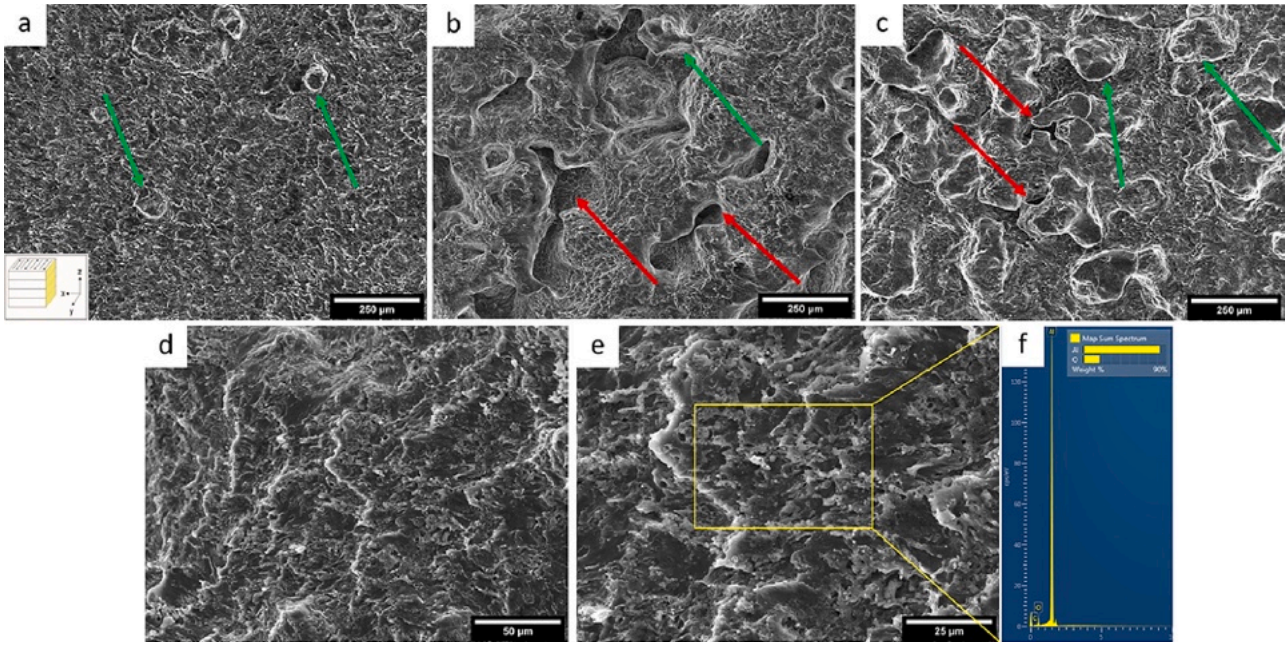

Fig. 3. SEM images of the lateral LSPed surfaces at the build direction of (a) S01, (b) S05 and (c) S07; (d) high magnification of the LSPed S01 surface; (e) and (f) are EDS of the LSPed S01 surface. The images show the main flaws: spatters (green arrows) and cavities (red arrows) on the surface after LSP treatment.

surface colored and a layer of aluminum oxide on the surface; which could be attributed to the type of confinement used during the LSP treatment (water and the plasma induced laser-material interaction) and subsequent formation of aluminum oxide on the surface.

3.2. Topography of the surfaces

Surface topography of the AB and LSPed surfaces and their corresponding surface parameters are presented in Fig. 4 and Fig. 5, respectively. According to data presented in Fig. 4, the LSPed surfaces generally show narrower height distribution. Thus, S01 surface features a distribution skewed towards positive values indicating surface dominated by peaks as the small valleys. After the LSP treatments, skewness reduced associated with narrower peak. On the contrary, LSPed S05 and S07 surfaces give significantly a shift towards negative (valleys) height distribution. This observation supported by SEM images presented in Fig. 2 and Fig. 3.

Typical areal surface parameters based on ISO 25178-2 [5-7] were calculated based on data collected from all microscopy measurements. The surface parameters were selected to evaluate the applicability of using specific LSP process on the AB surfaces: arithmetic mean height of the S-surface (Sa), maximum depth (Sv) and developed interfacial area ratio (Sdr).

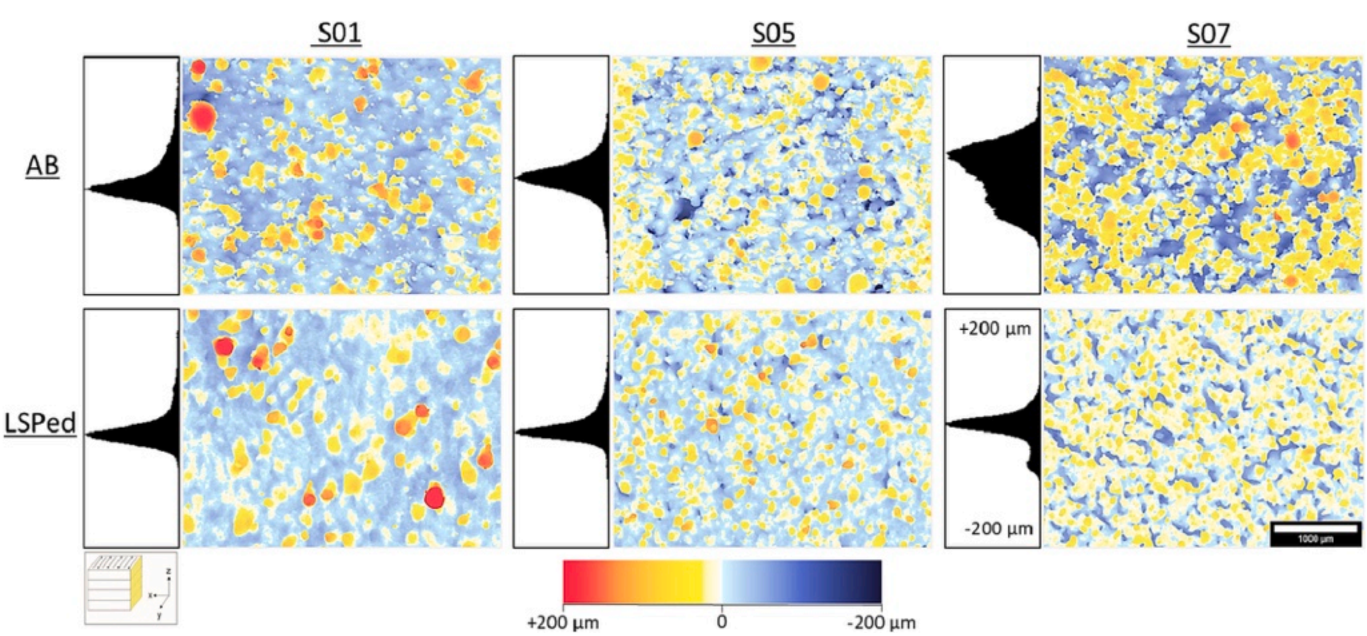

Fig. 4. Lateral surface topography obtained from confocal microscopy of AB surfaces (top row) and LSPed surfaces (bottom row) of S01, S05 and S07 specimens. Height distribution for each surface is presented with a normalized frequency curve for all surfaces. The image scale is identical for all the surfaces.

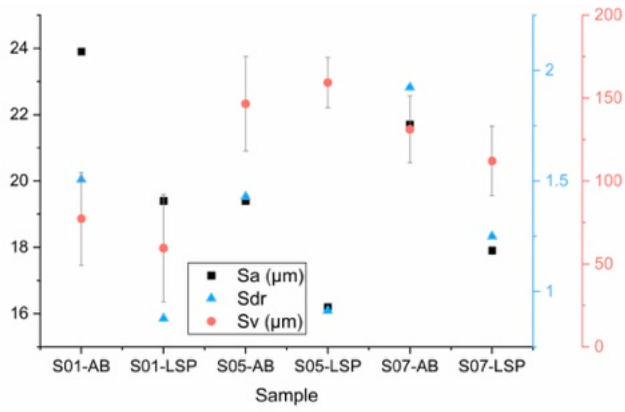

Fig. 5. Surface parameters: (a) Arithmetical mean height Sa, (b) Maximum valley depth Sv and (c) Developed interfacial area ratio Sdr, measured by confocal microscopy.

Among the parameters, Sv is known to represent the deepest notch found on the surface, which has been shown to correlate with the fatigue life [7,21]. Therefore, each area was divided into control areas and Sv was extracted from these small areas to improve the statistics. The measurements were done on three specimens to get more reliable results. Furthermore, the Sdr represents the additional surface area due to the presence of surface anomalies compared to the perfectly flat (Sdr = 0). It is worth to mention that conventional surface topography measurement methods such as optical focus variation or confocal microscopy have limited ability to measure the re-entrant surface features such as overhangs and undercuts, they can be considered as “line-of-sight” techniques. Accordingly, data produced by such techniques generally creates a height map with a single z value corresponding to each (x,y) position. Therefore, the surfaces between these points are interpolated leaving hidden re-entrant surface features [62]. Nonetheless, LSPed surfaces show smaller Sdr values, suggesting the evolution towards flatness via the subsequent deformation of the AB surface peaks.

According to Fig. 5 and in agreement with qualitative evaluation resulting from confocal microscopy images, some improvement is observed after the LSP process for the AB surfaces with almost identical Sa and the same AB surface parameters, LSP shows more similar characteristics when compared with counterpart AB conditions. Statistical measurements show that the distribution of surface features does not significantly change after LSP.

3.3. Microstructure and surface profile analysis

The sample surface profiles were investigated by microstructure observation of polished cross-sections perpendicular to the build direction, which provided an overview of the surface and particular, surface features created by L-PBF and the effect of the LSP process on the features. As expected, the results of topographic examination of the AB surfaces exhibit diverse surface profiles in terms of continuity, sub-surface features and the corresponding frequency of occurrence. Re-entrant features such as overhangs and undercuts are easily visible from these surface profile images. S01-AB surface was also found with occasional presence of several attached powder particles which were mostly eliminated after the LSP process (Fig. 6a and b). S05-AB and S07-AB specimens displayed a significantly higher number of re-entrant features and more porous sub-surface profiles. S07-AB specimens. However, it is very clear that the LSP process was able to close a large number of these features, giving rise to a smoother surface (Fig. 6c and d).

Fig. 7a and b provide overviews of the re-entrant features in AB surfaces. These features are marked by red arrows. Moreover, closure effect imposed by LSP process is demonstrated in Fig. 7c–f. From extensive cross-sectional observations, it was found that the region plastically affected by the LSP process has a depth of around 50 μm from the surface. The shock wave induced by LSP penetrates the surface and creates a multiaxial compressive stress region until its energy is dissipated [4,8]. The imposed compressive stresses also effectively close the re-entrant features, deforming the material out of the original regions and causes plastic deformation and pore closures (see Fig. 7e).

The grain structure of the AB and LSPed specimens are shown in the EBSD images presented in Fig. 8, with the examined area of 700 × 300 μm². The non-indexed porosities are shown in black. The grain structure of AB specimens is columnar with narrow

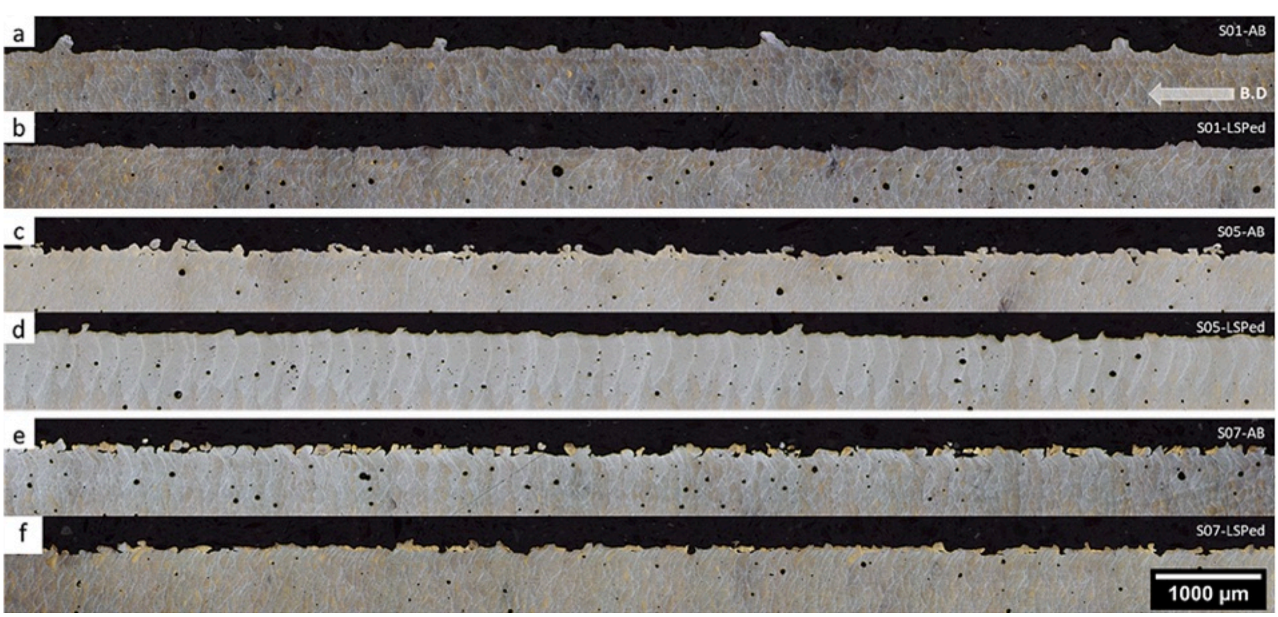

Fig. 6. Transverse cross-sections of specimens taken by OM: (a and b) S01-AB and LSPed surface, (c and d) S05-AB and LSPed surface, (e and f) S07-AB and LSPed surface. The profile length is 12 mm and the build direction is along the horizontal axis of the image (see white arrow in Fig. 6a).

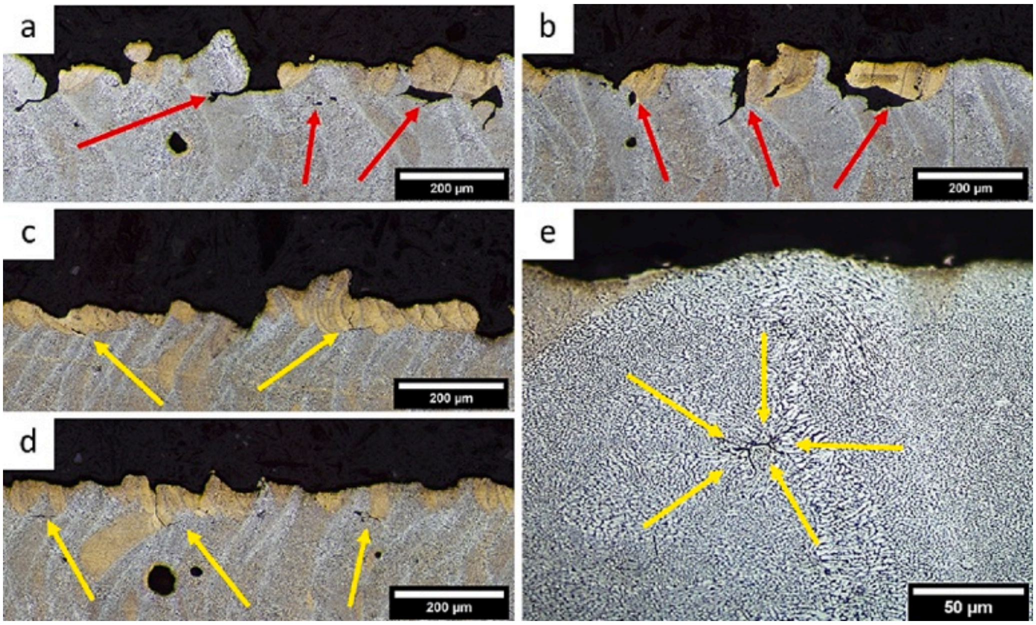

Fig. 7. Transverse view of S07 AB and LSP cubic specimens: (a and b) presence of near-surface closed sub-surface pores in AB surface (these features shown by red arrows); (c and d) closure of near-surface sub-surface pores after LSP process; (e) high magnification image of closed sub-surface pore after LSP process (these features shown by yellow arrows). (For interpretation of the references to colour in this figure legend, the reader is referred to the web version of this article.)

grains along the build direction. A similar structure was observed for the LSP specimens. However, the region very close to the surface (down to 40 µm below the surface) had a change in grain shape as it became evident as a result of LSP. The average grain aspect ratio in the vicinity of the surface (area of 700 × 40 µm²) was calculated via the Aztec Crystal software (Oxford Instruments). The average grain aspect ratio of 6.9, 5.8 and 6.5 for S01, S05 and S07 specimens in AB condition were measured. However, after the LSP treatment, the average grain aspect ratio of 4.6, 4.1 and 4.8 were reported, respectively, i.e. 33% - 26% decrease in this value.

3.4. Microhardness measurements

Fig. 9 presents the microhardness profiles of surfaces from the depth of 50 µm to 1.5 mm inside the bulk of the specimens. Plastic deformation induced strain-hardening during the LSP process slightly increased the hardness (around 10%) in the region close to the surface to a maximum depth of 300 µm. The effect of strain-hardening was lower in S07 surface due to the hollow sub-surface features. It complies with the fact that a significant portion of the energy from each pulse is spent to deform and close the cavities at the surface.

3.5. Residual stress measurement via hole drilling

Fig. 10 displays the evolution of the residual stresses throughout 1 mm thick layers from surface of AB and LSP samples. As expected, for AB condition, the tensile residual stress is inherent to the L-PBF as a result of solidification and thermal treatment and the corresponding graphs of S05 and S07 specimens exhibit very similar residual stress values in the region close to the surface, however, S01 specimen showed significantly lower tensile residual values. The significant increment in the compressive residual stress of AB S07 very close to the surface is due to the presence of excessive pores or peaks in the contour, incorporating the long axial distribution of solidification process as well as the high scanning speed (S05 and S07) and resulting in high level of overlapping tensile stresses in shrinkage consolidation [63]. Upon application of LSP and imposed shock waves from surface towards the bulk of sample, the compressive residual stresses have reached their maximum value at the surface region and decreasing through the thickness at a point when

the highest compressive residual stress in S01-LSP specimen shows the highest value of the compressive stress compared to LSP S05 and S07 units. This could be attributed to the lower number of voids and cavities on the surface of S01 specimens which would result in the absorbance and transmission of a larger portion of the LSP energy compared to porous surfaces with low density near surface region (S05 and S07). It also suggests that the porous regions that had already released stresses, have been rebound by pore closure resulting in greater relaxation of surface region after the LSP treatment.

3.6. X-ray micro-computed tomography

Representative micro-CT reconstructed plots of the near-surface region of the specimens in AB and LSP conditions are illustrated in Fig. 11. The sub-surface region magnified to better represent that the surface-connected sub-surface pores in AB conditions closed after the corresponding LSP treatment. It is confirmed that LSP was able to eliminate a large number of sub-surface pores in all three conditions. However, this effect was more pronounced in S05 and S07 surfaces due to the higher presence of sub-surface pores in AB condition. Moreover, the regions further away from the surface were not affected by the LSP induced plastic deformation. Furthermore, the deep sub-surface features remained present after the LSP treatment, which is in line with the optical microscopy measurements on the subspecimens.

3.7. Fatigue results

The results of three-point bending fatigue tests of AB [7] and LSP specimens are illustrated in Fig. 12. The tests to be repeated exhibit a limited scatter in the fatigue results. AB fatigue results from the previous study [7] showed a slight enhancement in the fatigue characteristics of this surface despite its significant texture. As it is expected, LSP fatigue results demonstrate the trend between the surface variability and the stress levels which could result in distinct approximately fatigue improvement. An improvement in the range of 50–80 MPa was observed in the fatigue limit of LSP specimens which correlates well with the change in residual stresses measured on the subspecimens by hole drilling.

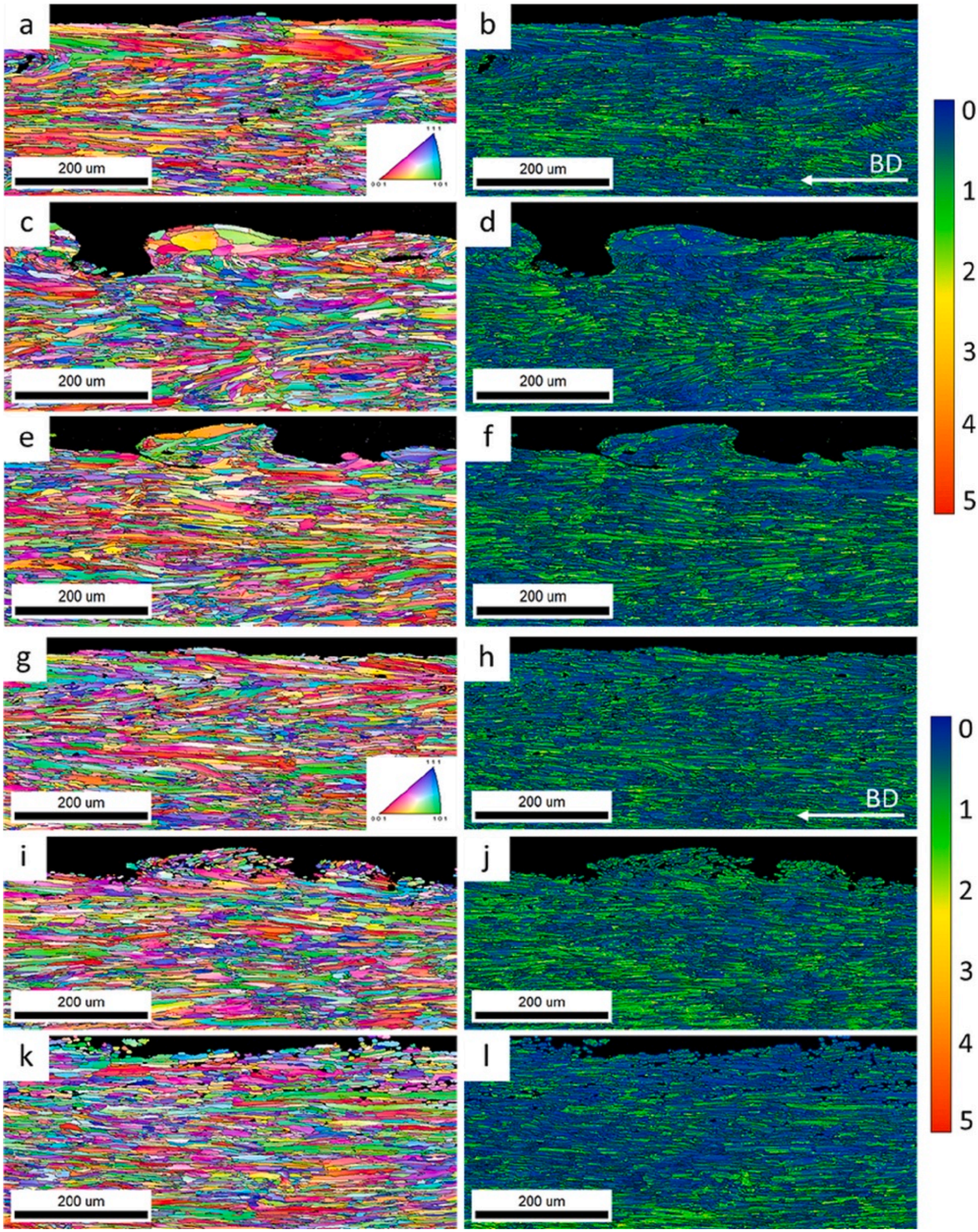

Fig. 8. EBSD inverse pole figures and Kernel average misorientation (KAM) maps of: (a, b) S01-AB, (c, d) S05-AB, (e, f) S07-AB, (g, h) S01-LSP, (i, j) S05-LSP, and (k, l) S07-LSP.

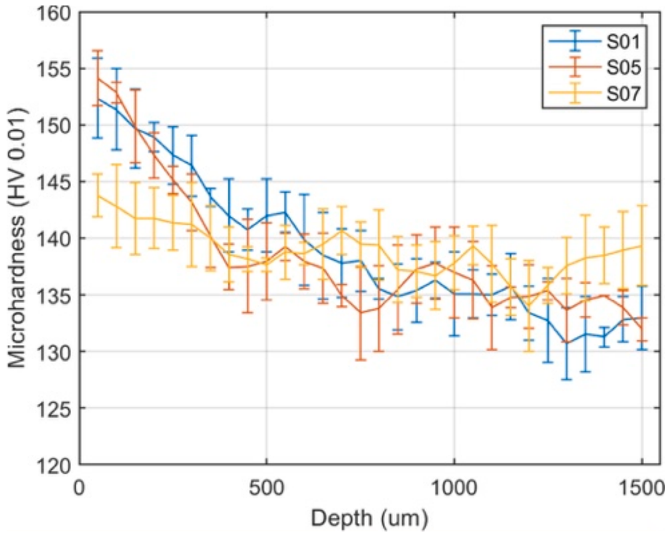

Fig. 9. Microhardness profile along the depth of the specimens from the three S01, S05 and S07 surfaces.

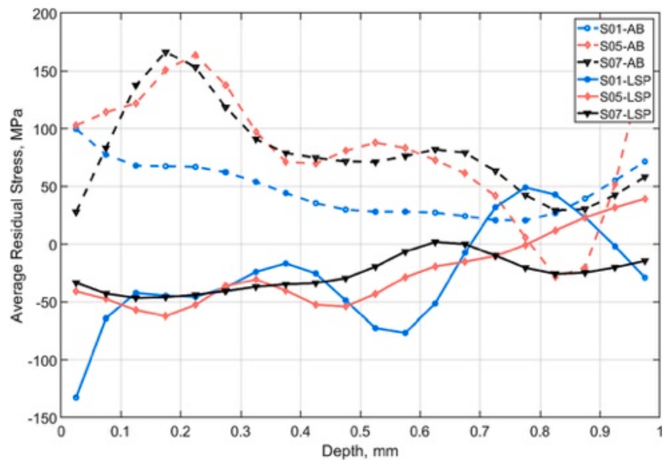

Fig. 10. Average residual stresses measured below the AB surfaces (dashed lines) and LSP-ed surfaces (solid lines).

3.8. Fractography

Based on the post-mortem analyses performed in the previous study on the AB specimens S01, S05 and S07 surfaces [7], all the failures occur from the surface or subsurface though some volume defects lie in the surface region. After a careful study of the LSP-ed fractured surfaces, it is noticeable that surface induced failures are surveyed (see Table 4). The failure tended to move towards surface defects with the result of LSP ability to close the sub-surface defects, exposing the surface notches as the failure initiation sites. In S01 LSP-ed specimens (see Fig. 13) failures from surface defects 67% occur, while no failure occurred in S01-AB specimens from the surface. S05 LSP-ed surfaces (see Fig. 14) exhibit 43% occurrence of failure via surface defects, similar to that of AB counterparts. S05 LSP-ed specimens usually fail through principal crack nucleation at surface under high stress ranges. S07 LSP-ed (see Fig. 15) showed an occasional failure from bulk defects but mostly failed through the defects originated from the surface regions.

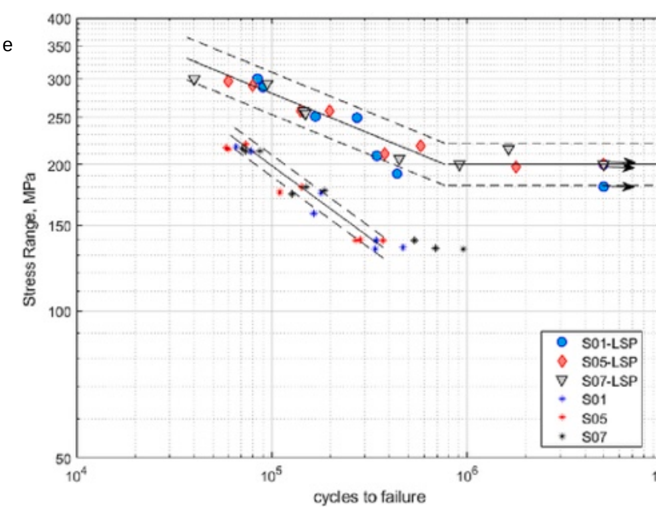

Fig. 12. Results of the fatigue tests of AB surfaces (star marks) [7] and LSP-ed surfaces (closed markers on top).

Table 4
Fracture origin of failures due to surface defects in AB and LSP-ed fatigue specimens.

Surface code	As-built (adopted from previous work [7])	LSP
S01	0%	67%
S05	44–55%	43%
S07	67–78%	90%

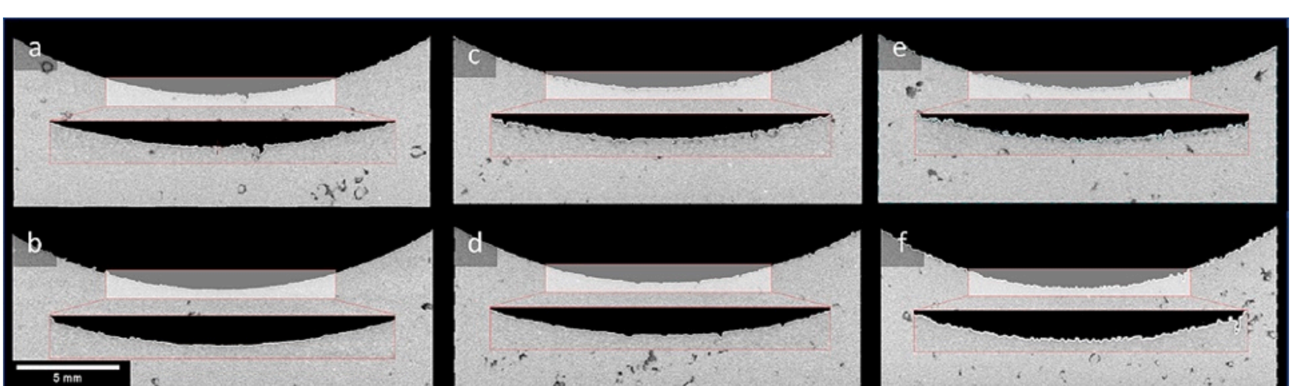

Fig. 11. micro-CT planar snapshots of the fatigue specimens in the corresponding gauge region of AB surfaces (a, c and e – above) and LSP-ed surfaces (b, d and f – below) of S01 (a and b), S05 (c and d) and S07 (e and f) specimens.

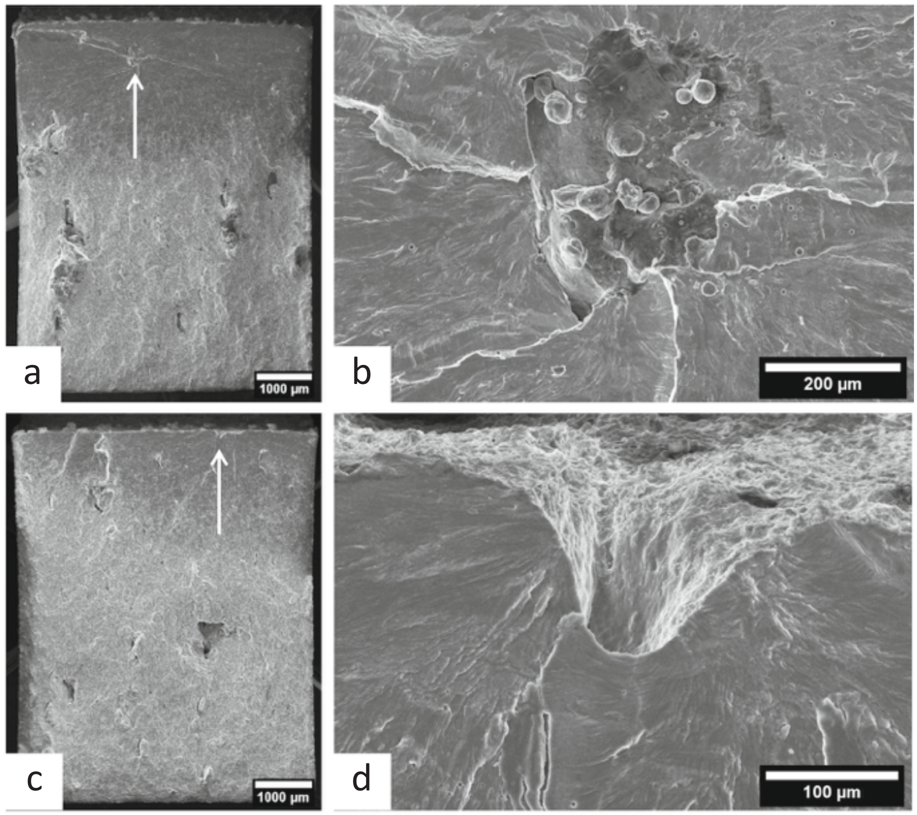

Fig. 13. SEM views of the fracture surfaces of S01-LSP specimens that failed from bulk and surface defects at stress ranges of (a and b) 220 MPa via bulk defect and (c and d) 300 MPa via surface defect. The white arrows indicate the crack initiation sites.

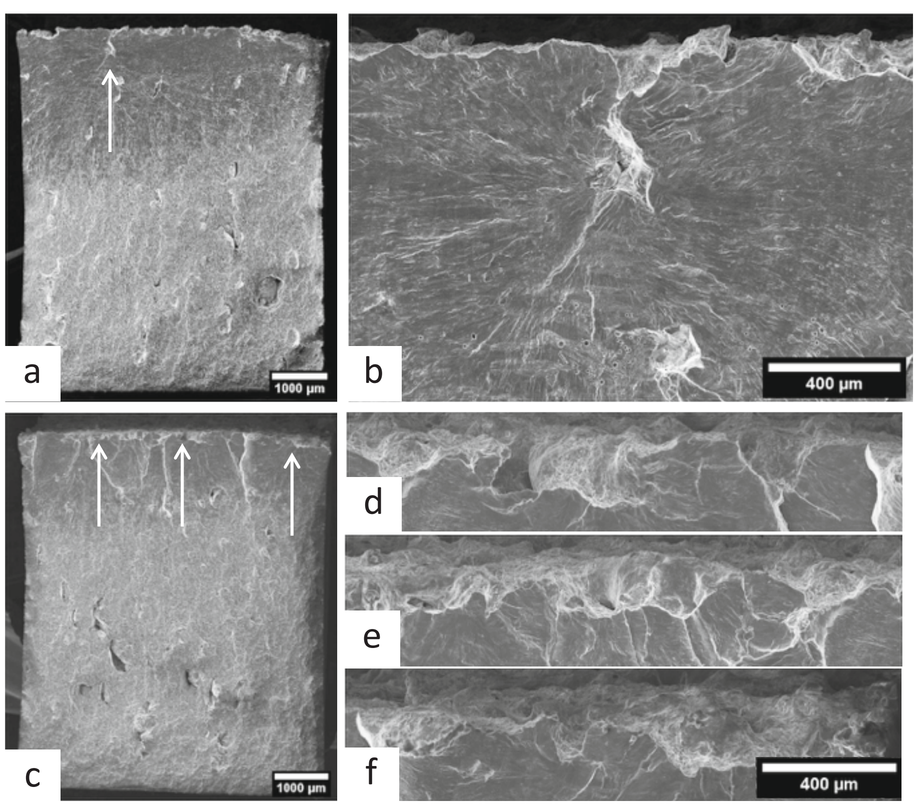

Fig. 14. SEM views of the fracture surfaces of S05-LSP specimens that failed from bulk and surface defects at stress ranges of (a and b) 220 MPa failed via single initiation site and (c and d) 300 MPa failed via multiple initiation sites. The white arrows indicate the crack initiation sites.

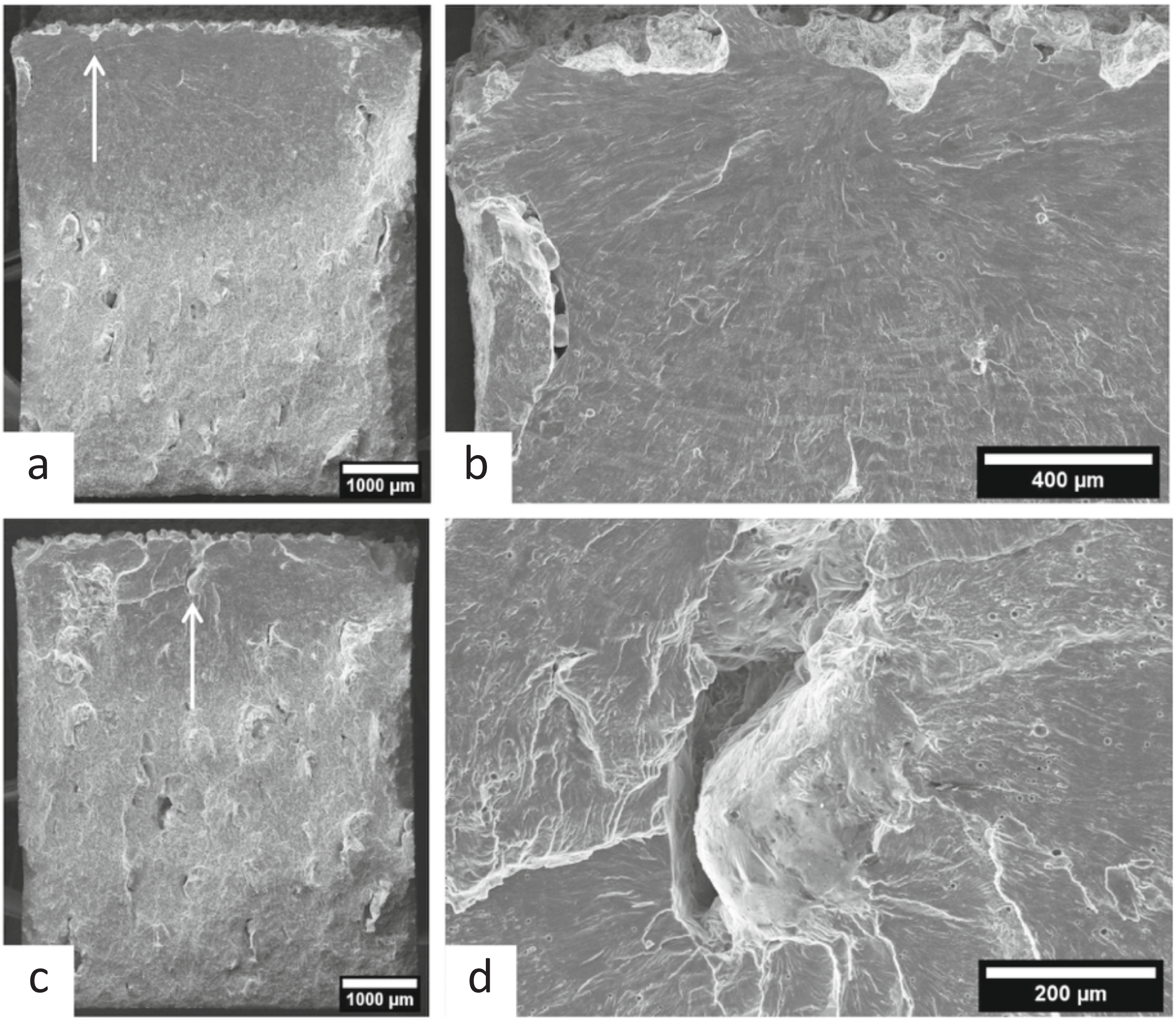

Fig. 15. SEM views of the fracture surfaces of two 307-LSP specimens that failed due to surface and subsurface defects at stress ranges of (a and b) 220 MPa failed via surface defect and (c and d) 300 MPa failed via subsurface defect. The white arrows indicate the crack initiation site.

4. Analysis of the fatigue test results

A comprehensive analysis of the fatigue data of the LSP specimens would be out of the scope of the present work since a large number of different factors potentially play a role in fatigue performance. First, there is a significant difference of the surface

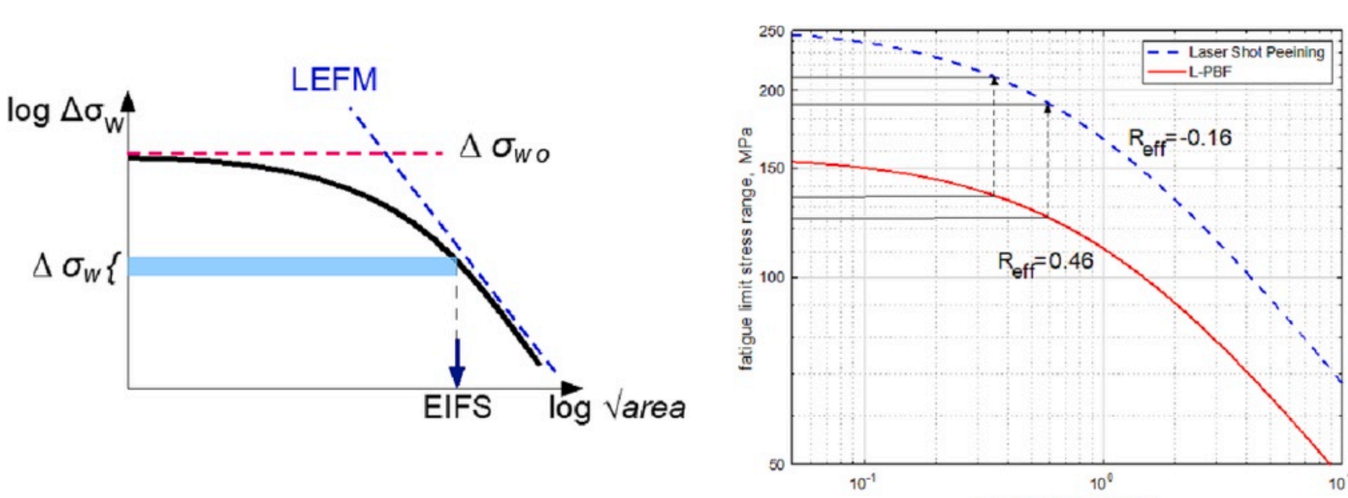

Fig. 16. The model of fatigue strength (a) and EIFS scheme (b) estimation of the fatigue limit for AM-B to LSP specimens.

to the presence of many surface defects [7] and the retained residual stresses. Since CT scans of the specimens were performed after the fatigue test [10] for every specimen, since it is the fatigue life controlling parameter. Based on the CT scans and the shape of the features that cause crack initiating during the fatigue test (see Fig. 13b) are elongated along the laser track (see Fig. 14d–e) pit-like feature (see Fig. 13d).

Therefore, since the main effect of LSP is on the significant change in surface defects (see Fig. 5), we decided to adopt an Equivalent Initial Flaw Size (EIFS) model [13,64], as depicted in Fig. 10a, where an equivalent defect size is calculated from the experimental fatigue limit.

It has been shown by many literature that the surface defect features treated by short-crack methods, or by different models [9], as simple yet predictive approaches for the fatigue strength to obtain the simple method by combining El-Haddad [65] with Murakami's model of stress intensity factor (SIF) [66] to determine the fatigue limit as expressed by [15]:

$$\Delta\sigma_{\omega} = \Delta\sigma_{\omega o}\cdot\sqrt{\frac{\sqrt{area_o}}{\sqrt{area}+\sqrt{area_o}}} \quad (2)$$

where:

$$\sqrt{area_o} = \frac{1}{\pi}\left(\frac{\Delta K_{th}}{F.\Delta\sigma_{\omega o}}\right)^2 \quad (3)$$

The El-Haddad parameters are $\sqrt{area_o}$ and $F = 0.65$ for surface defects [67]. The two material parameters in Eq. (2) are ΔK_{th} and ΔS_{wo}, being the long crack threshold and the fatigue limit of smooth specimens, respectively [68]. The key point in applying this concept is to correct it by considering the effective stress due to the presence of residual stresses [15,46].

Considering the presence of residual stresses, AB and LSP samples exhibit residual stress (σ_{res}) values of +100 MPa and −50 MPa respectively at 100 μm below the surface. The effective stress ratio (R_{eff}) can be computed considering the experimentally obtained fatigue limit and values of residual stress at the surface for both AB and LSP specimens presented in Table 5.

The applying fatigue strength model that need different material parameters from AlSi10Mg (fatigue tests on AlSi7Mg are quite close to AlSi10Mg), specific fatigue limit at different stress ratios is shown in Fig. 10b, where the defect size has been normalized to $\sqrt{area}$. For the fatigue limit $\Delta S_w = 130$ MPa at $R_{eff} = 0.46$ in the AB samples, and the range of 190–210 MPa at $R_{eff} = -0.16$ for LSP specimens, which is perfectly in line with experimental results.

This simple analysis shows that, apart from modification of the internal voids [36], the main effect of LSP is introducing compressive residual stresses to significantly enhance the fatigue strength [22,46].

Finally, some aspects should be considered for a complete analysis of influencing factors (which): slight increase in hardness measured in this investigation might produce modification of fatigue strength; possible relaxation of residual stresses during the work-hardening in the experimental fatigue tests of the samples. Both these effects are assumed to be negligible with the considered conditions and thus not accounted for in the model.

5. Conclusions

The effect of LSP and different surface conditions on specimens of L-PBF AlSi7Mg is investigated here. Samples were processed with different process parameters to obtain a variety of surface and microstructures resulting in diverse surface profiles with different characteristics. The quality of the

Table 5
Comparison of fatigue limits and the corresponding effective stress ratios.

	LSP	AB
Fatigue limit stress range	200 [MPa]	130 [MPa]
Effective stress ratio (R_{eff})	−0.16	0.46

LSP and surface were investigated through surface analysis utilizing SEM/EDS (general morphology and chemical composition of surface as a result of LSP treatment), confocal microscopy (quantifying the variation in surface features such as peaks and valleys), polished cross-sections (allowing to observe sub-surface features and internal porosity that are possible to be observed through optical microscopy), hole drilling (measuring the residual stresses) from the surface to a depth of 1 mm in LSP and AB samples. The LSP condition was applied to L-PBF fatigue specimens and qualitatively correlated with fractography on SEM of the fatigue specimens and analysis of the subsequent specimens on SEM, EDS, and CT. Analyses were performed on LSP fatigue specimens to evaluate the effect of LSP treatment on the external surface. The fracture surfaces were carefully investigated after performing fatigue tests on three sets of specimens. Furthermore, simple fracture mechanics analysis revealed the dominant effect of residual stresses on the fatigue improvement in LSP specimens.

The following conclusions are drawn:

- No significant change in surface roughness was observed after LSP, while the laser peening induced deep compressive residual stresses through the sample;
- The closure of near-surface features and sub-surface porosity was achieved after the LSP treatment, confirmed on polished section and CT scan analysis;
- Laser peening resulted in microstructural changes at 50 μm below the surface as a deformation while no measurable change in grain shape (as a result of LSP), with a slight increase in micro-hardness subsurface up to a depth of about 300 μm;
- The fatigue strength of LSP specimens improved substantially (by about 50% compared to AB specimens). Such increase can be attributed to the beneficial effect of compressive residual stresses.

Declaration of Competing Interest

The authors declare that they have no known competing financial interests or personal relationships that could have appeared to influence the work reported in this paper.

Data availability

Data will be made available on request.

Acknowledgements

The support by the Italian Ministry of Education, University and Research (MIUR) through the project "Department of Excellence LIS4.0 - Integrated Laboratory for Lightweight e-Smart Structures" is acknowledged. Authors would like to acknowledge Dr. Charlotte Frommer for her kind assistance in the review process.

References

[1] T. DebRoy, H.L. Wei, J.S. Zuback, T. Mukherjee, J.W. Elmer, J.O. Milewski, A.M. Beese, A. Wilson-Heid, A. De, W. Zhang, Additive manufacturing of metallic components – process, structure and properties, Prog. Mater. Sci. 92 (2018) 112–224, https://doi.org/10.1016/j.pmatsci.2017
[2] D. Herzog, V. Seyda, E. Wycisk, C. Emmelmann, Additive manufacturing of metals, Acta Mater. (2016), https://doi.org/10.1016/j.actamat.

[3] D.D. Gu, W. Meiners, K. Wissenbach, R. Poprawe, Laser additive manufacturing of metallic components: materials, processes and mechanisms, Int. Mater. Rev. 57 (2012) 133–164, https://doi.org/10.1179/1743280411Y.0000000014.

[4] N. Sohrabi, J. Jhabvala, R.E. Logé, Additive manufacturing of metallic glasses - process, challenges and perspectives, Metals (Basel) 11 (2021) 1279, https://doi.org/10.3390/met11081279.

[5] M. Hamidi Nasab, M. Vedani, E. Bionda, R.E. Logé, A Study on the Surface Features of the SLM Process and Their Journey to Become Defects, Euro. Powder Metall. Assoc. 2019.

[6] J.-P. Kruth, J. Deckers, E. Yasa, R. Wauthlé, Assessing and comparing influencing factors of residual stresses in selective laser melting using a novel analysis method, Proc. Inst. Mech. Eng. Part B J. Eng. Manuf. 226 (2012) 980–991, https://doi.org/10.1177/0954405412437085.

[7] M. Hamidi Nasab, S. Romano, D. Gastaldi, S. Beretta, M. Vedani, Combined effect of surface anomalies and volumetric defects on fatigue assessment of AlSi7Mg fabricated via laser powder bed fusion, Addit. Manuf. 34 (2020), https://doi.org/10.1016/j.addma.2019.100918.

[8] N. Sohrabi, M. Hamidi-Nasab, B. Rheingans, J. Jhabvala, A. Parrilli, M. Vedani, R.E. Logé, Fatigue performance of additively manufactured Zr-based bulk metallic glass and the effect of post-processing, Metals 11 (2021), https://doi.org/10.3390/met11071064.

[9] M. Hamidi Nasab, G. Giussani, D. Gastaldi, V. Tirelli, M. Vedani, Effect of surface and subsurface defects on fatigue behavior of AlSi10Mg alloy processed by laser powder bed fusion (L-PBF), Metals (Basel) 9 (2019) 1063, https://doi.org/10.3390/met9101063.

[10] M. Hamidi Nasab, D. Gastaldi, N.F. Lecis, M. Vedani, On morphological surface features of the parts printed by selective laser melting (SLM), Addit. Manuf. 24 (2018) 373–377, https://doi.org/10.1016/j.addma.2018.10.011.

[11] U. Zerbst, G. Bruno, J.-Y. Buffière, T. Wegener, T. Niendorf, T. Wu, X. Zhang, N. Kashaev, G. Meneghetti, N. Hrabe, M. Madia, T. Werner, K. Hilgenberg, M. Koukolíková, R. Procházka, J. Džugan, B. Möller, S. Beretta, A. Evans, R. Wagener, K. Schnabel, Damage tolerant design of additively manufactured metallic components subjected to cyclic loading: state of the art and challenges, Prog. Mater. Sci. 121 (2021) 100786, https://doi.org/10.1016/j.pmatsci.2021.100786.

[12] A. du Plessis, S. Beretta, Killer notches: the effect of as-built surface roughness on fatigue failure in AlSi10Mg produced by laser powder bed fusion, Addit. Manuf. 35 (2020) 101424, https://doi.org/10.1016/j.addma.2020.101424.

[13] S. Beretta, M. Gargourimotlagh, S. Foletti, A. du Plessis, M. Riccio, Fatigue strength assessment of "as built" AlSi10Mg manufactured by SLM with different build orientations, Int. J. Fatigue 139 (2020) 105737, https://doi.org/10.1016/j.ijfatigue.2020.105737.

[14] M. Hamidi Nasab, F. Alzate, A. Redaelli, N. Lecis, A. Giussani, L. Smail, M. Vedani, Finishing treatment of external surfaces produced by Powder Bed Fusion: SI: G, Addit. Manuf. 2017.

[15] E. Maleki, S. Bagherifard, S.M.J. Razavi, M. Riccio, M. Bandini, A. du Plessis, F. Berto, M. Guagliano, Fatigue behaviour of notched laser powder bed fusion AlSi10Mg after thermal and mechanical surface post-processing, Mater. Sci. Eng. A 829 (2022) 142145, https://doi.org/10.1016/j.msea.2021.142145.

[16] W.H. Kan, Y. Nadot, M. Foley, L. Ridosz, G. Proust, J.M. Cairney, Factors that affect the properties of additively-manufactured AlSi10Mg: porosity versus microstructure, Addit. Manuf. 29 (2019) 100805, https://doi.org/10.1016/j.addma.2019.100805.

[17] A. du Plessis, E. Macdonald, Hot isostatic pressing in metal additive manufacturing: X-ray tomography reveals details of pore closure, Addit. Manuf. 34 (2020), 101191, https://doi.org/10.1016/j.addma.2020.101191.

[18] S. Tammas-Williams, P.J. Withers, I. Todd, P.B. Prangnell, The effectiveness of hot isostatic pressing for closing porosity in titanium parts manufactured by selective electron beam melting, Metall. Mater. Trans. A 47 (2016) 1939–1946, https://doi.org/10.1007/s11661-016-3429-3.

[19] J.J. Lewandowski, M. Seifi, Metal additive manufacturing: a review of mechanical properties, Annu. Rev. Mater. Res. 46 (2016) 151–186.

[20] E. Maleki, S. Bagherifard, M. Bandini, M. Guagliano, Surface post-treatments for metal additive manufacturing: progress, challenges, and opportunities, Addit. Manuf. 37 (2021) 101619, https://doi.org/10.1016/J.ADDMA.2020.101619.

[21] M. Hamidi Nasab, G. Giussani, D. Gastaldi, V. Tirelli, M. Vedani, Effect of surface and subsurface defects on fatigue behavior of AlSi10Mg alloy processed by laser powder bed fusion (L-PBF), Metals (Basel) 9 (2019) 1063, https://doi.org/10.3390/met9101063.

[22] M. Benedetti, E. Torresani, M. Leoni, V. Fontanari, M. Bandini, C. Pederzolli, C. Potrich, The effect of post-sintering treatments on the fatigue and biological behavior of Ti-6Al-4V ELI parts made by selective laser melting, J. Mech. Behav. Biomed. Mater. 71 (2017) 295–306, https://doi.org/10.1016/j.jmbbm.2017.03.024.

[23] L. Hackel, J.R. Rankin, A. Rubenchik, W.E. King, M. Matthews, Laser peening: a tool for additive manufacturing post-processing, Addit. Manuf. 24 (2018) 67–75, https://doi.org/10.1016/j.addma.2018.09.013.

[24] S. Luo, W. He, K. Chen, X. Nie, L. Zhou, Y. Li, Regain the fatigue strength of laser additive manufactured Ti alloy via laser shock peening, J. Alloys Compd. 750 (2018) 626–635, https://doi.org/10.1016/j.jallcom.2018.04.029.

[25] P. Yella, K.V. Rajulapati, G.V. Prasad Reddy, R. Sandhya, P.P. Kiran, K. Buddu, K. Bhanu Sankara Rao, Effect of laser shock peening on high cycle fatigue characteristics of 316LN stainless steel, Int. J. Press. Vessel. Pip. 176 (2019) 103972, https://doi.org/10.1016/j.ijpvp.2019.103972.

[26] S. Huang, Z. Zhao, J. Sheng, X. Meng, E. Agyenim-Boateng, D. Ma, J. Lu, J. Zhou, Effect of laser peening with different power densities on vibration fatigue resistance of hydrogen-charged TC4 titanium alloy, Int. J. Fatigue 131 (2020) 105335, https://doi.org/10.1016/j.ijfatigue.2019.10

[27] K. Yang, Q. Huang, B. Zhong, Q. Wang, Q. Chen, Y. Chen, N. Su, H. Liu, Enhanced extra-long life fatigue resistance of a bimodal titanium alloy by laser shock peening, Int. J. Fatigue 141 (2020) 105868, https://doi.org/10.1016/j.ijfatigue.2020.105868.

[28] M. Kemal Kulekci, U. Esme, Critical analysis of processes and apparatus for industrial surface peening technologies, Int. J. Adv. Manuf. Technol. 74 (2014) 1551–1565, https://doi.org/10.1007/s00170-014-60

[29] N.E. Uzan, S. Ramati, R. Shneck, N. Frage, O. Yeheskel, On the effect of shot-peening on fatigue resistance of AlSi10Mg specimens fabricated by additive manufacturing using selective laser melting (AM-SLM), Addit. Manuf. 21 (2018) 458–464, https://doi.org/10.1016/J.ADDMA.2018.0

[30] J. Damon, S. Dietrich, F. Vollert, J. Gibmeier, V. Schulze, Process dependent porosity and the influence of shot peening on porosity morphology regarding selective laser melted AlSi10Mg parts, Addit. Manuf. 20 (2018) 77–89, https://doi.org/10.1016/J.ADDMA.2018.01.001.

[31] D. Chadwick, S. Ghanbari, D.F. Bahr, M.D. Sangid, Crack incubation in shot peened AA7050 and mechanism for fatigue enhancement, Fatigue Fract. Eng. Mater. Struct. 41 (2018) 71–83, https://doi.org/10.1111/ffe.12652.

[32] M. Munther, T. Martin, A. Tajyar, L. Hackel, A. Beheshti, K. Davami, Laser shock peening and its effects on microstructure and properties of additively manufactured metal alloys: a review, Eng. Res. Express 2 (2020), 022001, https://doi.org/10.1088/2631-8695/ab9b16.

[33] N. Kalentics, E. Boillat, P. Peyre, S. Ćirić-Kostić, N. Bogojević, R.E. Logé, Tailoring residual stress profile of selective laser melted parts by laser shock peening, Addit. Manuf. (2017), https://doi.org/10.1016/j.addma.2017

[34] E. Maleki, S. Bagherifard, O. Unal, M. Bandini, M. Guagliano, On the effects of laser shot peening on fatigue behavior of V-notched AlSi10Mg manufactured by laser powder bed fusion, Int. J. Fatigue 163 (2022) 107035, https://doi.org/10.1016/j.ijfatigue.2022.107035.

[35] N. Kalentics, M.O.V. de Seijas, S. Griffiths, C. Leinenbach, R.E. Logé, 3D laser shock peening – a new method for improving fatigue properties of selective laser melted parts, Addit. Manuf. 33 (2020) 101112, https://doi.org/10.1016/j.addma.2020.101112.

[36] Q. Jiang, S. Li, C. Zhou, B. Zhang, Y. Zhang, Effects of laser shock peening on the ultra-high cycle fatigue performance of additively manufactured Ti6Al4V alloy, Opt. Laser Technol. 144 (2021) 107391, https://doi.org/10.1016/j.optlastec.2021.107391.

[37] Y. Jing, X. Fang, N. Xi, X. Feng, K. Huang, Investigation of microstructure and mechanical properties evolution of 7050 aluminum alloy and 316L stainless steel treated by laser shock peening, Mater. Charact. 182 (2021) 111571, https://doi.org/10.1016/j.matchar.2021.111571.

[38] J. Lu, H. Lu, X. Xu, J. Yao, J. Cai, K. Luo, High-performance integrated additive manufacturing with laser shock peening–induced microstructural evolution and improvement in mechanical properties of Ti6Al4V alloy components, Int. J. Mach. Tools Manuf. 148 (2020) 103475, https://doi.org/10.1016/j.ijmachtools.2019.103475.

[39] N. Kalentics, A. Burn, M. Cloots, R.E. Logé, 3D laser shock peening as a way to improve geometrical accuracy in selective laser melting, Int. J. Adv. Manuf. Technol. 101 (2019) 1247–1254, https://doi.org/10.1007/s001

[40] W. Guo, R. Sun, B. Song, Y. Zhu, F. Li, Z. Che, B. Li, C. Guo, L. Liu, P. Peng, Laser shock peening of laser additive manufactured Ti6Al4V titanium alloy, Surf. Coat. Technol. 349 (2018) 503–510, https://doi.org/10.1016/j.sur

[41] L. Chen, P. Gu, T. Ge, Y. Sun, L. Li, X. Ren, Effect of laser shock peening on microstructure and mechanical properties of TiC strengthened Inconel 625 alloy processed by selective laser melting, Mater. Sci. Eng. A 835 (2022) 142610, https://doi.org/10.1016/j.msea.2022.142610.

[42] C. Wang, L. Wang, C.-L. Wang, K. Li, X.-G. Wang, Dislocation density-based study of grain refinement induced by laser shock peening, Opt. Laser Technol. 121 (2020) 105827, https://doi.org/10.1016/j.optlastec

[43] R. Sun, L. Li, Y. Zhu, W. Guo, P. Peng, B. Cong, J. Sun, Z. Che, B. Li, C. Guo, L. Liu, Microstructure, residual stress and tensile properties control of wire-arc additive manufactured 2319 aluminum alloy with laser shock peening, J. Alloys Compd. 747 (2018) 255–265, https://doi.org/10.1016/j.jallcom

[44] H. Zhang, Z. Cai, J. Chi, G. Han, R. Sun, Z. Che, H. Zhang, W. Guo, Microstructural evolution, mechanical behavior and strengthening mechanism of 300M steel subjected to multi-pass laser shock peening, Opt. Laser Technol. 148 (2022), 107726, https://doi.org/10.1016/j.optlastec.202

[45] L. Lan, X. Jin, S. Gao, B. He, Y. Rong, Microstructural evolution and stress state related to mechanical properties of electron beam melted Ti-6Al-4V alloy modified by laser shock peening, J. Mater. Sci. Technol. 50 (2020) 153–161, https://doi.org/10.1016/j.jmst.2019.11.039.

[46] N. Kalentics, K. Huang, M. Ortega Varela de Seijas, A. Burn, V. Romano, R.E. Logé, Laser shock peening: a promising tool for tailoring metallic microstructures in selective laser melting, J. Mater. Process. Technol. 266 (2019) 612–618, https://doi.org/10.1016/j.jmatprotec.2018.11.024.

[47] M. Morgano, N. Kalentics, C. Carminati, J. Capek, M. Makowska, R. Woracek, T. Maimaitiyili, T. Shinohara, R. Loge, M. Strobl, Investigation of the effect of laser shock peening in additively manufactured samples through Bragg edge neutron imaging, Addit. Manuf. 34 (2020) 101201, https://doi.org/10.1016/j.addma.2020.101201.

[48] A. du Plessis, D. Glaser, H. Moller, N. Mathe, L. Tshabalala, B. Mfusi, R. Mostert, Pore closure effect of laser shock peening of additively manufactured AlSi10Mg, 3D Print. Addit. Manuf. 6 (2019) 245–252, https://doi.org/10.1089/3

[49] P. Yella, K.V. Rajulapati, G.V. Prasad Reddy, R. Sandhya, P. Prem Kiran, R.K. Buddu, K. Bhanu Sankara Rao, Effect of laser shock peening on high cycle fatigue characteristics of 316LN stainless steel, Int. J. Press. Vessel. Pip. 176 (2019) 103972, https://doi.org/10.1016/j.ijpvp.2019.103972.
[50] S. Huang, J. Zhao, J. Sheng, X. Meng, E. Agyenim-Boateng, D. Ma, J. Lu, J. Zhou, Effect of laser peening with different power densities on vibration fatigue resistance of hydrogen-charged TC4 titanium alloy, Int. J. Fatigue 131 (2020) 105335, https://doi.org/10.1016/j.ijfatigue.2019.105335.
[51] K. Yang, Q. Huang, B. Zhong, Q. Wang, Q. Chen, Y. Chen, N. Su, H. Li, Enhanced extra-long life fatigue resistance of a bimodal titanium alloy by laser shock peening, Int. J. Fatigue 141 (2020) 105868, https://doi.org/10.1016/j.ijfatigue.2020.105868.
[52] Z. Qin, B. Li, X. Huang, H. Zhang, C. Chen, M. Adeel, H. Xue, The effect of laser shock peening on surface integrity and high and very high cycle fatigue properties of 2024-T351 aluminum alloy, Opt. Laser Technol. 149 (2022) 107897, https://doi.org/10.1016/j.optlastec.2022.107897.
[53] D. Courapied, L. Berthe, P. Peyre, F. Coste, J.-P. Zou, A.-M. Sautivet, Laser-delayed double shock-wave generation in water-confinement regime, J. Laser Appl. (2015), https://doi.org/10.2351/1.4906382.
[54] N.J. Rendler, I. Vigness, Hole-drilling strain-gage method of measuring residual stresses, Exp. Mech. 6 (1966) 577–586, https://doi.org/10.1007/BF02326825.
[55] ASTM International, ASTM E837-20, Standard Test Method for Determining Residual Stresses by the Hole-Drilling Strain-Gage Method, 2021.
[56] A. Thompson, N. Senin, I. Maskery, L. Körner, S. Lawes, R. Leach, Internal surface measurement of metal powder bed fusion parts, Addit. Manuf. 20 (2018) 126–133, https://doi.org/10.1016/j.addma.2018.01.003.
[57] International Organization for Standardization, ISO 25178-2, Geometrical Product Specifications (GPS) – Surface Texture: Areal – Part 2: Terms, Definitions and Surface Texture Parameters, 2007.
[58] G.T. Smith, Machined surface integrity, in: G.T. Smith (Ed.), Industrial Metrology: Surfaces and Roundness, Springer, London, 2002, pp. 185–247, https://doi.org/10.1007/978-1-4471-3814-3_5.
[59] L. Boniotti, S. Beretta, L. Patriarca, L. Rigoni, S. Foletti, Experimental and numerical investigation on compressive fatigue strength of lattice structures of AlSi7Mg manufactured by SLM, Int. J. Fatigue (2019), https://doi.org/10.1016/j.ijfatigue.2019.06.041.
[60] R. Casati, M. Vedani, Aging response of an A357 Al alloy processed by selective laser melting, Adv. Eng. Mater. (2018) 1800406, https://doi.org/10.1002/adem.201800406.
[61] A. du Plessis, S.G. le Roux, A. Guelpa, The CT scanner facility at Stellenbosch University: an open access X-ray computed tomography laboratory, Nucl. Instrum. Methods Phys. Res. Sect. B Beam Interact. Mater. Atoms 384 (2016) 42–49, https://doi.org/10.1016/j.nimb.2016.08.0
[62] A. Townsend, L. Pagani, P. Scott, L. Blunt, Introduction of a surface characterization parameter Sdr prime for analysis of re-entrant features, J. Nondestruct. Eval. (2019), https://doi.org/10.1007/s1092
[63] N.C. Levkulich, S.L. Semiatin, J.E. Gockel, J.R. Middendorf, A.T. DeWald, N.W. Klingbeil, The effect of process parameters on residual stress evolution and distortion in the laser powder bed fusion of Ti-6Al-4V, Addit. Manuf. 28 (2019) 475–484, https://doi.org/10.1016/j.addma.2019.0
[64] Y. Liu, S. Mahadevan, Probabilistic fatigue life prediction using an equivalent initial flaw size distribution, Int. J. Fatigue 31 (2009) 476–487, https://doi.org/10.1016/j.ijfatigue.2008.06.005.
[65] M.H. El Haddad, K.N. Smith, T.H. Topper, Fatigue crack propagation of short cracks, J. Eng. Mater. Technol. 101 (1979) 42–46, https://doi.org/10.1115/1.3443647.
[66] Y. Murakami, S. Beretta, SIF and threshold for small cracks at small notches under torsion, Fatigue Fract. Eng. Mater. Struct. 23 (2000) 97–104, https://doi.org/10.1046/j.1460-2695.2000.00260.x.
[67] Y. Murakami, Chapter 2 - Stress concentration, in: Y. Murakami (Ed.), Metal Fatigue, Elsevier Science Ltd, Oxford, 2002, pp. 11–24, https://doi.org/10.1016/B978-008044064-4/50002-5.
[68] K.J. Miller, The short crack problem, Fatigue Fract. Eng. Mater. Struct. (1982), https://doi.org/10.1111/j.1460-2695.1982.tb